The Astrophysical Journal, 889:132 (12pp), 2020 February 1 https://doi.org/10.3847/1538-4357/ab65f6

The Physical Properties of S0 Galaxy PGC 26218: The Origin of Starburst and Star Formation

Xue Ge[1,2,3], Qiu-Sheng Gu[1,2,3], Rubén García-Benito[4], Meng-Yuan Xiao[1,2,3], and Zong-Nan Li[1,2,3]
[1] School of Astronomy and Space Science, Nanjing University, Nanjing, Jiangsu 210093, People's Republic of China; qsgu@nju.edu.cn
[2] Key Laboratory of Modern Astronomy and Astrophysics (Nanjing University), Ministry of Education, Nanjing, Jiangsu 210093, People's Republic of China
[3] Collaborative Innovation Center of Modern Astronomy and Space Exploration, Nanjing, Jiangsu 210093, People's Republic of China
[4] Instituto de Astrofísica de Andalucía (CSIC), P.O. Box 3004, E-18080 Granada, Spain
Received 2019 July 26; revised 2019 December 24; accepted 2019 December 27; published 2020 January 31

Abstract

We present 2D-spectroscopic observations from the Centro Astronómico Hispano Alemán 3.5 m telescope and millimeter observations from the NOrthern Extended Millimeter Array of the nearby S0 galaxy PGC 26218, which shows central star formation activity and post-starburst features in the disk. We estimate the star formation rate (SFR $= 0.28 \pm 0.01\ M_{\odot}\ \mathrm{yr}^{-1}$) and molecular gas mass ($\log M_{\mathrm{H_2}} = 7.60 \pm 0.15\ M_{\odot}$) of PGC 26218 based on the extinction-corrected Hα emission line and the CO–H_2 conversion factor (α_{CO}) of the Milky Way, respectively. We find that PGC 26218 follows the star-forming main sequence (SFMS) and the Kennicutt–Schmidt law. Comparing the kinematics of CO($J = 1$–0), stars, and Hα, we find that the rotational axis of CO($J = 1$–0) is 45° different from that of Hα. In addition, the profile of the CO($J = 1$–0) emission line shows asymmetry and has an inflow component of $\sim$46 km s^{-1}. With the decomposition of the optical image, we confirm that PGC 26218 shows multiple nuclear structures. The projected offset between the most luminous optical center and the center of CO($J = 1$–0) is 5.″2 ($\sim$0.6 kpc) and the latter overlaps with one of the optical cores. These results indicate that PGC 26218 may have experienced a gas-rich minor merger, extending its star formation and locating it in the SFMS.

Unified Astronomy Thesaurus concepts: Starburst galaxies (1570); Star formation (1569); Lenticular galaxies (915)

1. Introduction

Lenticular galaxies (S0s) are typically considered to be the intermediate transition population between spiral and elliptical galaxies in the Hubble tuning fork diagram (Hubble 1936). They are classified as early-type galaxies (ETGs) based on their morphology. The prominent features in S0 galaxies are the absence of spiral arms and noticeable star formation regions.

Some formation scenarios for S0 galaxies have been proposed. On the one hand, S0 galaxies can be formed by the morphological transformation of spiral galaxies, which consume the gas in their disks (Bedregal 2007; Bekki & Couch 2011; Kormendy & Bender 2012; Johnston et al. 2014; Rizzo et al. 2018). On the other hand, external effects, such as galaxy harassments (Moore et al. 1996), tidal encounters in high-density environments and cluster gravitational potential wells (Bekki 1998; Moore et al. 1998; Aragón-Salamanca et al. 2006; Governato et al. 2009; Laurikainen et al. 2010), and galaxy mergers (Aguerri et al. 2001; Eliche-Moral et al. 2006; Querejeta et al. 2015; Tapia et al. 2017) may also lead to the formation of S0 galaxies. In addition, the existence of a bar may also play an important role in the formation of S0 galaxies via gas transport to the center, fueling a starburst (Laurikainen et al. 2006). A recent study has shown that a violent disk instability could also be an important forming mechanism of S0 galaxies (Saha & Cortesi 2018). Generally, S0 galaxies are gas-poor, inactive galaxies. They likely formed through a combination of multiple processes due to the diverse properties in their bulges and disks (Laurikainen et al. 2010; Barway et al. 2013; Fraser-McKelvie et al. 2018) and help us understand the diverse evolutionary paths from star-forming blue galaxies to quiescent red galaxies.

Although S0 galaxies are often thought to have evolved passively after a big burst of star formation, some studies found that these galaxies still have nuclear star formation activity (Kaviraj et al. 2007; Schawinski et al. 2007). Further studies have found that neutral and even molecular gas is present in most S0 galaxies (van Driel & van Woerden 1991; Welch & Sage 2003; Sage & Welch 2006; Welch et al. 2010). This reservoir of gas could be explained via gas-rich mergers (Davis et al. 2015) and gas accretion from the environment (Dressler et al. 2013). In addition, *N*-body simulations show that stellar mass loss can also fuel residual star formation in massive ETGs (Jungwiert et al. 2001).

Based on the revised Third Reference Catalog of Bright Galaxies (RC3, Lee & Brunner 2015) and Sloan Digital Sky Survey (SDSS) Data Release 7 (Abazajian et al. 2009), Xiao et al. (2016) collected a visual morphology sample of S0 galaxies. They presented the properties of nuclear activities for the sample of S0 galaxies and found that 45 (8%) nearby S0 galaxies show signs of nuclear star formation activity. In order to understand the nature and spatially resolved properties of this sample of star-forming S0 galaxies, we have started a program to obtain Integral Field Spectroscopy data with the Centro Astronómico Hispano Alemán (CAHA) 3.5 m telescope. SDSS J091705.28+252545.4 (PGC 26218) is one of the observed star-forming S0 galaxies ($z = 0.00548$). Figure 1 shows the SDSS composite color image. We can see the disturbed structure and a bright star-forming knot in the center of PGC 26218. In order to investigate the molecular gas in this S0 galaxy, we observed the CO($J = 1$–0) emission line with the NOrthern Extended Millimeter Array (NOEMA). Our main purpose in this paper is to determine the origins of star formation in PGC 26218 and whether such an S0 galaxy follows the star formation laws of normal star-forming galaxies.

The paper is organized as follows. Sections 2 and 3 show the observations and data analysis of optical Integral Field Unit

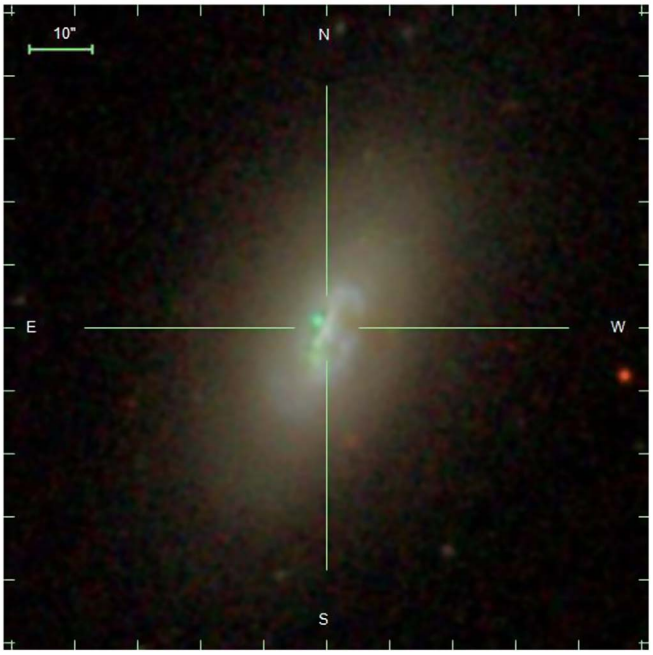

Figure 1. SDSS *gri* image of PGC 26218 where $1'' \sim 0.11$ kpc.

(IFU) and millimeter data. Section 4 gives our results and discussions, including the star formation in PGC 26218 in the context of the star-forming main sequence (SFMS) and the Kennicutt–Schmidt (K–S) law, the kinematics of stars and gas, and the origins of star formation. In Sections 5, we present our summary. Throughout the paper, we adopt a cosmology with $\Omega_M = 0.3$, $\Omega_\Lambda = 0.7$, and $H = 70\,\mathrm{km\,s^{-1}\,Mpc^{-1}}$ and a Salpeter (1955) initial mass function (IMF).

2. Observations and Data Reductions

In this section, we present our observations and reductions of optical spectroscopy and millimeter data. Based on the preliminary analysis, we aim to give the reader a general perception of the nearby S0 galaxy PGC 26218. The archival parameters and the results from the data analysis for PGC 26218 are summarized in Tables 1 and 2, respectively.

2.1. CAHA 2D-spectroscopic Observations

We obtained optical IFU spectroscopic observations of PGC 26218 from CAHA on 2016 March 11 and 12. The 3.5 m telescope covers two optical overlapping setups. The red spectrograph covers the wavelength range from 3745 to 7500 Å with a low spectral resolution ($R \sim 850$, V500), while the blue covers the wavelength range from 3400 to 4840 Å with a medium spectral resolution ($R \sim 1650$, V1200). In order to obtain a filling factor of 100%, a three-pointing dithering scheme was used. The exposure time per pointing was 900 s for the red (taken on the first day) and 1800 s for the V1200 (split in two individual exposures of 900 s). We used a Python-based pipeline for reduction of the PPAK data based on an upgraded version of García-Benito et al. (2015) and Sánchez et al. (2016). The reduction process can be summarized in the following steps: identification of the position of the spectra on the detector along the dispersion axis; extraction of each individual spectrum; distortion correction of the extracted spectra; wavelength calibration; fiber-to-fiber transmission correction; flux-calibration; sky-subtraction; cube reconstruction; and

Table 1
The Archival Parameters of PGC 26218

PGC 26218	
R.A. (SDSS) [J2000.0]	139.272017
Decl. (SDSS) [J2000.0]	25.429165
Redshift (SDSS)	0.00548
$\log M_*$ ($M_\odot$) (MPA-JHU DR7[a])	$9.32^{s}/9.15^{k}$

Note. The superscript "s" on the stellar mass indicates that the stellar mass was computed adopting a Salpeter (1955) IMF, while "k" denotes a Kroupa (2001) IMF.
[a] https://wwwmpa.mpa-garching.mpg.de/SDSS/DR7/

Table 2
A Summary of the Physical Properties for PGC 26218

PGC 26218	
A_v (mag)	0.76 ± 0.06
$\log$ SFR ($M_\odot\ \mathrm{yr^{-1}}$)	-0.55 ± 0.01
$\log \Sigma_{\mathrm{SFR}}$ ($M_\odot\ \mathrm{yr^{-1}\ kpc^{-2}}$)	-1.39 ± 0.01
Inclination (deg)	64.5
b/a	0.49
$12 + \log$ (O/H)	8.53 ± 0.13
$S_{\mathrm{CO}\,(J=1-0)}\,\Delta v$ ($\mathrm{Jy\ km\ s^{-1}}$)	6.78 ± 0.75
$\log L'_{\mathrm{CO}\,(J=1-0)}$ ($\mathrm{K\ km\ s^{-1}\ pc^2}$)	6.96 ± 0.75
$\log M_{\mathrm{H_2}}$ ($M_\odot$)	7.60 ± 0.15
$\log \Sigma_{\mathrm{gas}}$ ($M_\odot\ \mathrm{pc^{-2}}$)	1.30 ± 0.14
$\log \Sigma_1$ ($M_\odot\ \mathrm{kpc^{-2}}$)	8.25

finally differential atmospheric correction. To reduce the effects of vignetting on blue part (up to ~4200 Å) of the V500 data in some parts of the field of view (FOV); (see Figure 11 of Husemann et al. 2013), we combine both setups producing a so-called COMBO data cube. The V1200 spectral resolution is degraded to match the V500 data. We then combine the data from both data sets averaging the V1200 cube and V500 cube in the overlapping wavelength range, weighted by the inverse of the error. For the remaining wavelength range, the blue part corresponds to the matched V1200 cube and the red part to the right of the overlapping region to the original V500 data cube. More details of the reduction process can be found in Husemann et al. (2013), García-Benito et al. (2015) and Sánchez et al. (2016). The final data cube, corrected for Galactic extinction, fully covers the optical range from 3700 to 7300 Å.

2.2. The Fitting of Stellar Continuum and Emission Lines

Preprocessed spectral data (78×73 spaxels) are stored in a 3D data cube. We first bin the 2D spectral data to a constrained signal-to-noise ratio (S/N) with the Voronoi binning method (Cappellari & Copin 2003). We adopt the average flux and the standard deviation of the flux as the signal and noise at the wavelength range from 5075 to 5125 Å. This range is not contaminated by emission and absorption lines. Spaxels below a lower S/N limit set by us are stacked together with neighboring spaxels until they satisfy the required minimum S/N. We tested several realizations with S/N = 5, 10, and 20 and finally adopted S/N = 10 in this work. Although higher S/N is better for the fitting, this will reduce the number of spaxels and smooth the details in space. This process produces 1370 Voronoi bins with S/N higher than 10, 80% of which include only one spaxel. Next, we use the pPXF code (Cappellari & Emsellem 2004; Cappellari 2017), a stellar

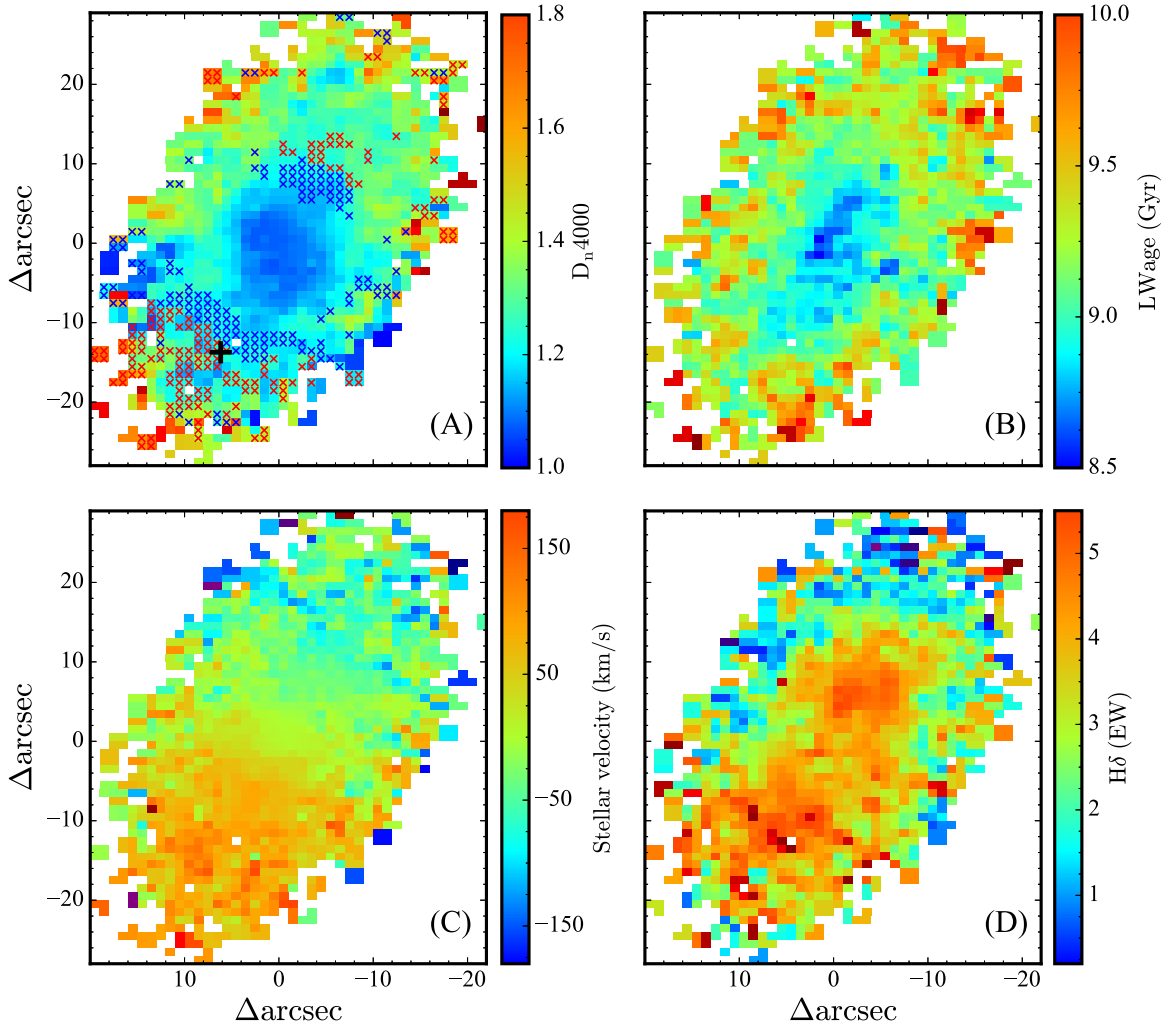

Figure 2. Distributions of optical parameters color coded by D_n4000 (A), light-weighted age (B), velocity (C), and EW (of Hδ, (D)), respectively. The positive value in EW denotes absorption. The map center is set at R.A., decl. = 139.272, 25.429 and $1''\sim 0.11$ kpc. In panel (A), the red and blue crosses represent quiescent post-starburst and transiting post-starburst regions, respectively, based on the EW of Hα and Hδ. The black cross indicates the center of millimeter observations.

population analysis method, to fit the stellar continuum, during which the emission lines are masked (Hα, [O III], Hβ, etc.). The code adopts MILES simple stellar population templates (Sánchez-Blázquez et al. 2006; Vazdekis et al. 2010), assuming a Salpeter (1955) IMF and a Calzetti et al. (2000) dust extinction curve, covering 25 population ages (between 0.06 and 15.85 Gyr) and 6 metallicities (log[M/H] = −1.71, −1.31, −0.71, −0.4, 0.0, 0.22). All spectra are fitted in the wavelength range from 3800 to 7200 Å. We check visually all the fitting results and exclude some peculiar fits with stellar velocity dispersions higher than 400 km s^{-1} and D_n4000 (the ratio of continuum 4000–4100 and 3850–3950 Å, Balogh et al. 1999) higher than 2.0, which results in 1200 spectra analyzed in this work. We emphasize that the elimination of spaxels by the visual inspection process does not significantly affect our results.

Figure 2 shows the distributions of fitted parameters derived from pPXF. Panel (A) represents D_n4000, an indicator for stellar population age (Kauffmann et al. 2003b). The small value of D_n4000 implies that there is ongoing star formation in the central region. A similar trend can be found from the light-weighted age (panel (B)), which is weighted by the fraction of light for each template. Panel (C) represents the stellar velocity map, showing a characteristic rotated disk-shape structure. It is interesting that the equivalent width (EW, positive value represents absorption) of the Hδ line is large along the major axis (panel (D)), suggesting that these regions might have experienced a starburst process several hundred Myr ago.

For the emission lines, we subtract the estimated stellar continuum from the observed spectrum and obtain the line flux with the SHERPA IFU line fitting software (SHIFU; García-Benito, in preparation), based on the package CIAO SHERPA (Freeman et al. 2001; Doe et al. 2007). Small deviations with respect to the stellar continuum are taken into account by a first-order polynomial. Single Gaussians have been fitted for the emission lines and the width of the Gaussians were tied for ions of the same element.

2.3. The Selection of Regions with Different Star Formation Histories

PGC 26218 is a star-forming S0 galaxy and displays post-starburst (PSB) regions in the disk. In order to show the locations of regions with different star formation histories, we pick out these regions according to the EW of Hα and Hδ.

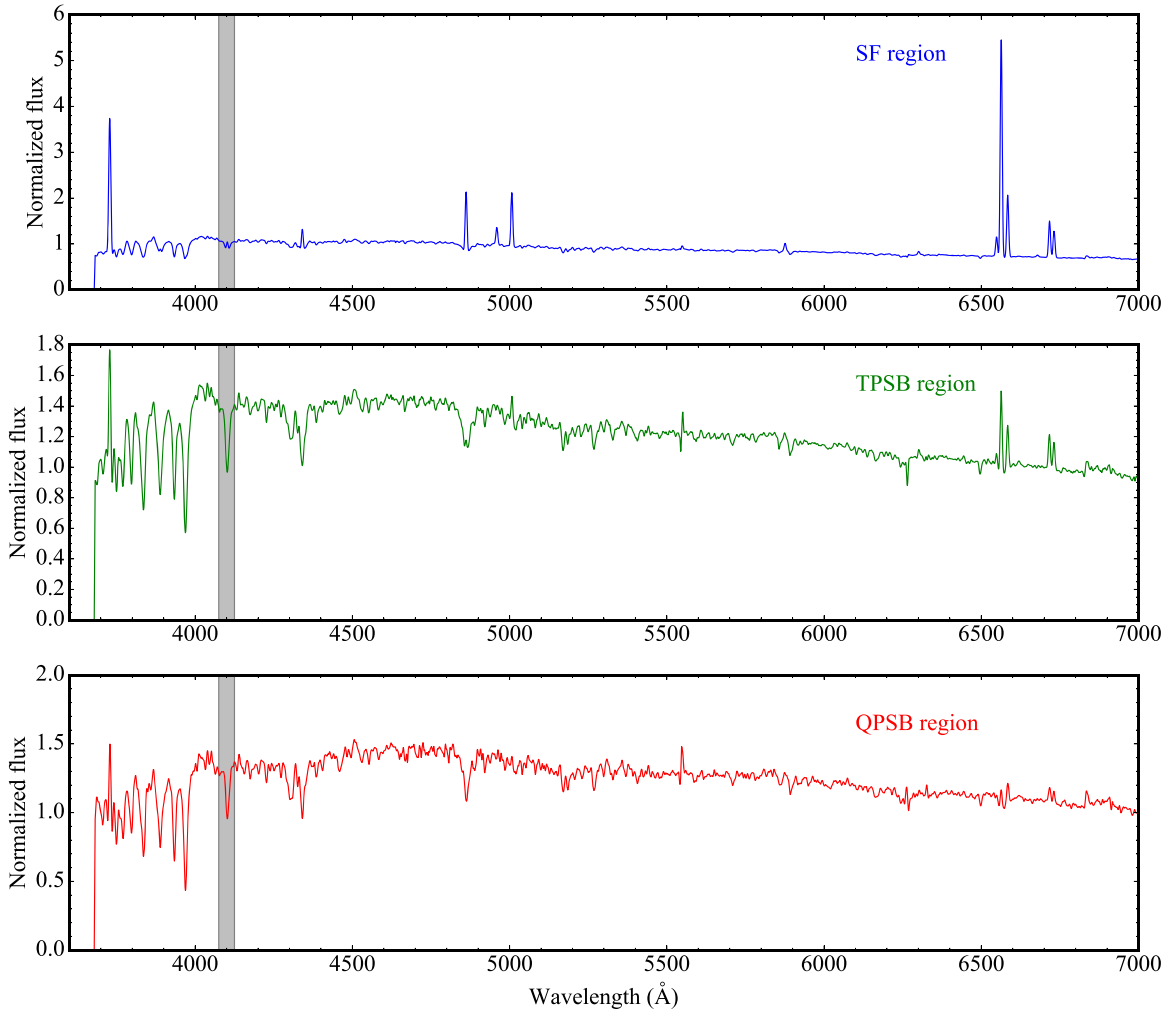

Figure 3. Stacked spectra for SF (top), TPSB (middle), and QPSB (bottom). All the spectra are normalized at 4100 Å. The shadow marks the region of Hδ.

A traditional picture of post-starburst galaxies is that these objects have experienced violent starbursts and then rapidly quenched star formation within the last few hundred Myr. Their optical spectra are characterized by strong Balmer absorption lines and weak nebular emission lines. Therefore, the post-starburst galaxies are usually selected based on the deficiency of emission lines (such as Hα or [O II]) and on strong Hδ absorption lines (Blake et al. 2004; Quintero et al. 2004; Goto 2005, 2007; Poggianti et al. 2009; Vergani et al. 2010). The strong high-order Balmer absorption lines are evidence of the existence of A-type stars, while the absence of emission lines indicates that there is no recent star formation in the past few Gyr.

The traditional definition for the post-starburst phase imposes a rigorous cut on Hα emission line (Balogh et al. 2005; Hogg et al. 2006). The restriction on Hα intensity may miss some post-starburst galaxies that reside in the early evolutionary phase. Recent studies show that the early stage is also important for understanding the evolution of post-starburst galaxies (Yesuf et al. 2014; Rowlands et al. 2015; Alatalo et al. 2016; Pawlik et al. 2018). In this work, the quiescent post-starburst regions (QPSB) are defined as EW (Hδ) > 4 Å and EW (Hα) > -3 Å, while the transitioning post-starburst regions (TPSB) are defined as EW (Hδ) > 4 Å and -10 Å $<$ EW (Hα) < -3 Å. For QPSB, the definition is the same as in Yesuf et al. (2014). The upper limit on EW (Hα) ensures that the TPSB region has only residual star formation. The typical errors for the EW of Hα and Hδ are 1.0 Å and 1.4 Å, respectively. The corresponding regions are marked in panel (A) of Figure 2. We find that the QPSB regions (red crosses) are mainly located outside 1.5 effective radii ($R_e \sim 13''$), while the TPSB regions (blue crosses) are mainly concentrated around the center of PGC 26218. Furthermore, we define the regions with EW (Hδ) < 4 Å and EW (Hα) < -3 Å or EW (Hδ) > 4 Å and EW (Hα) < -10 Å as the star-forming (SF) regions. We emphasize that the number of spaxels for QPSB accounts for 20% of the total spaxels of these three regions. This significant amount of QPSB spaxels shows that PGC 26218 has undergone a starburst several hundred Myr ago. Based on the optical features, millimeter observation coordinates (black cross) are selected between the two PSB regions. We will describe the CO($J = 1$–0) emission in Section 3.

Figure 3 shows the stacked spectra for SF, TPSB, and QPSB regions, respectively. For the spectrum of SF, it shows the strongest Hα emission and weakest Hδ absorption. The spectrum of TPSB has similar Hδ absorption but stronger Hα emission than that of QPSB. This feature might indicate that PGC 26218 needs a period of transition for the emission lines to fade from TPSB to QPSB.

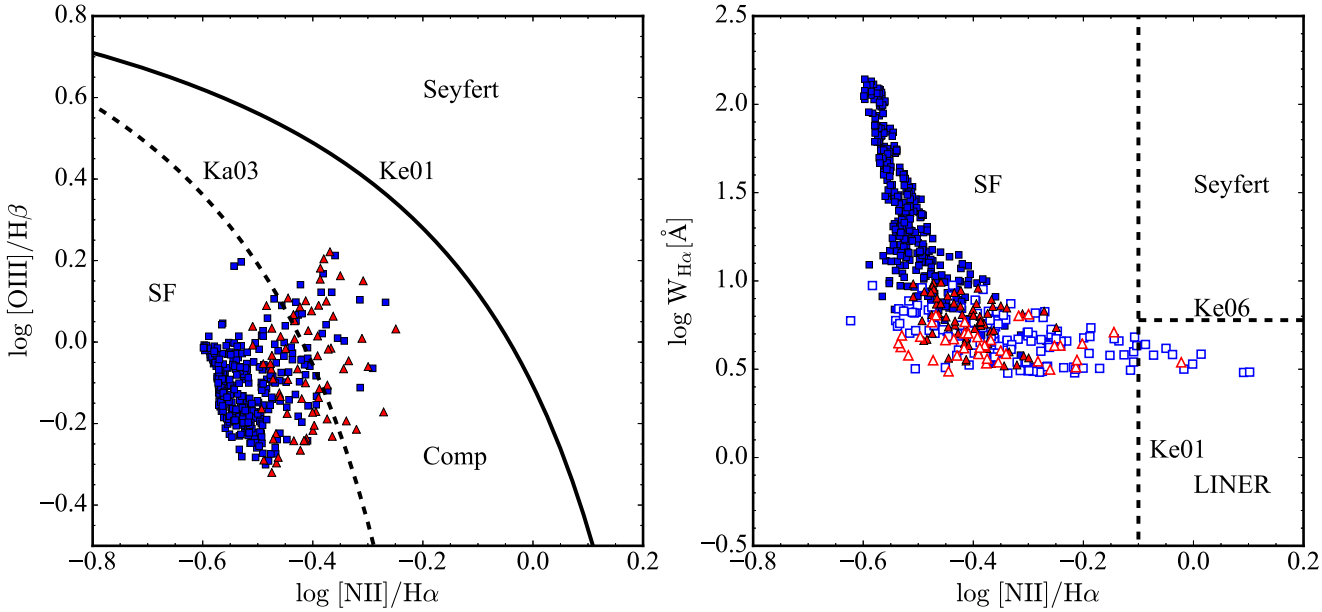

Figure 4. Left panel: the traditional BPT diagnostic diagram for SF and TPSB regions. The blue squares and red triangles represent the spaxels with S/N of four emission lines larger than 3 for SF and TPSB, respectively. The dashed and solid lines are from Kauffmann et al. (2003a) and Kewley et al. (2001), respectively. Right panel: an alternative diagnostic diagram of excitation mechanisms for SF and TPSB regions. The hollow squares and triangles represent the spaxels with S/N of Hβ or [O III] lower than 3 for SF and TPSB, respectively. The blue solid squares and red triangles are the same as in the left panel. The horizontal dashed line is from Kewley et al. (2006) and the vertical dashed line is from Kewley et al. (2001).

2.4. SFR, Gas-phase Metallicity, and $\Sigma_{H\,I}$

The emission lines may be contaminated by active galactic nuclei (AGNs) and shocks, which would lead to the overestimation of the star formation rate (SFR) when we use Hα as tracer of star formation. To this end, we investigate the excitation mechanisms for SF and TPSB regions according to the traditional BPT diagram (Baldwin et al. 1981, left panel of Figure 4). In this diagram, we impose the S/N of these four emission lines (i.e., Hα, [N II], Hβ, and [O III]) to be greater than 3. For the spaxels with Hα and [N II] S/N larger than 3, we use the relation between the EW (Hα) and [N II]/Hα (right panel of Figure 4) as the diagnostic diagram of excitation mechanisms (Cid Fernandes et al. 2010). We find no spaxels in the Seyfert region, which indicates that PGC 26218 does not host an AGN. Although some spaxels locate at the composite and LINER regions, the effect from shock is ignorable considering that most of the spaxels locate at the SF region and the contribution from shocks to emission lines could be low in the SF region. Taking into account that all of the SF and TPSB spaxels have EW(Hα) < -3 Å and the percent light contribution (at $\lambda = 5100$ Å) of young populations in those spaxels is larger than 4%, we believe that most of the contribution is dominated by ionization due to young stars and only a tiny fraction by hot low-mass evolved stars/post AGB stars (González Delgado et al. 2016; Lacerda et al. 2018). At any rate, our SFR value is an upper limit.

In order to estimate the spatially resolved SFR from extinction-corrected Hα emission lines, we calculate the extinction according the Balmer decrement assuming a Cardelli et al. (1989) extinction curve with case B condition for each Voronoi bin. The extinction-corrected SFR is calculated using the formula given by Kennicutt (1998a):

$$\mathrm{SFR}(M_\odot\ \mathrm{yr}^{-1}) = 7.9 \times 10^{-42} L(\mathrm{H}\alpha), \quad (1)$$

where L(Hα) is the extinction-corrected Hα luminosity. For the total extinction-corrected SFR, we construct a spectrum by stacking all spaxels in Voronoi bins of SF and TPSB regions. We use the pPXF code again to model the stellar continuum. For the continuum-subtracted emission-line spectrum, we simultaneously fit Hα, [N II], Hβ, and [O III] lines using the single Gaussian model (see Figure 5) and calculate the extinction. It is worth noting that the MPA/JHU SDSS DR7 catalog (Brinchmann et al. 2004) provided the aperture-corrected SFR of PGC 26218 (SFR $\sim 0.20\ M_\odot\ \mathrm{yr}^{-1}$) based on a Kroupa (2001) IMF, whereas we adopt a Salpeter (1955) IMF and find the total SFR is $\sim 0.28\ M_\odot\ \mathrm{yr}^{-1}$. The conversion between the two IMFs is Kroupa IMF $\times$ 1.5 $\approx$ Salpeter IMF. Therefore our SFR is consistent with that given by Brinchmann et al. (2004).

The inclination and axial ratio (see Table 2) derived from *GALFIT* (Version 3.0.5, Peng et al. 2002) show that the projection effect may affect the accuracy of surface densities. We calculate the inclination based on

$$i = \arccos\sqrt{\frac{q^2 - q_0^2}{1 - q_0^2}} \quad (2)$$

where $q = b/a$, the ratio of minor semiaxis and major semiaxis. We adopt $q_0 = 0.25$ (Sandage et al. 1970) instead of 0.2 (Hubble 1926) to correct the inclination for classical S0 galaxies. We find the inclination-corrected star formation rate surface density (Σ_{SFR}), also referred to as the intensity of the star formation, is lower by 0.3 dex than that of non-inclination-corrected Σ_{SFR}. However, the correction for the inclination will lead to an equal decrease in molecular gas surface density (Σ_{gas}). Thus, the inclination correction will only cause the parameters to move to the lower left in the K–S law, but will not significantly affect the results shown in Figure 9.

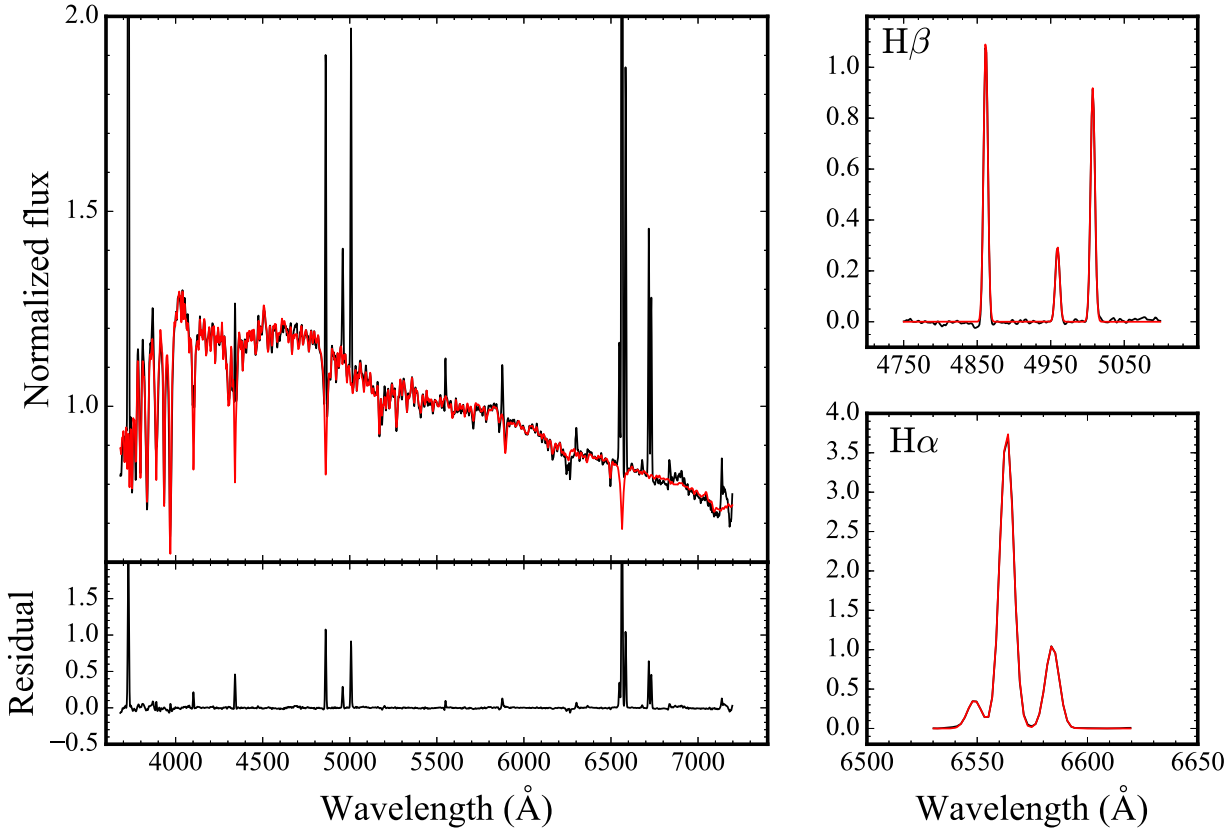

Figure 5. Left panels: results of pPXF 150 simple stellar population synthesis for the stacked spectrum of PGC 26218. The black and red curves are the original and the model spectra, respectively. The residual spectrum is shown at the bottom. Right panels: we highlight the single Gaussian fitting for Hβ and Hα. The black and red lines represent the original data and the model, respectively.

The gas-phase metallicity of PGC 26218 is derived based on the Bayesian method[5] (Blanc et al. 2015) with the Levesque et al. (2010) photoionization model, which allows us to input arbitrary sets of strong nebular emission lines to infer the probability density functions of gas-phase metallicity and ionization parameter. We use the spectra that are used to compute the SFR to estimate the gas-phase metallicity, which is $\sim 1\sigma$ below the relation derived by Tremonti et al. (2004) while consistent with the relation given by Sánchez et al. (2013) within the error range.

We use the average gas-phase metallicity (see Table 2) to derive the surface mass density of atomic gas ($\Sigma_{\rm H\,I}$) according to the empirical formula given by Schruba et al. (2018). In this scaling relation, the optically thin conversion is adopted and a factor of 1.36 is taken into account to include the heavy elements. Furthermore, the effects of diffuse H I on the saturation column density is neglected. However, the assumption does not significantly affect $\Sigma_{\rm H\,I}$.

3. NOEMA Millimeter Observations and Data Analysis

3.1. NOEMA Millimeter Observations

PGC 26218 was observed with NOEMA located in the south of the French Alps on 2018 June 16 (Project S18BN001. PI: Xue Ge). The source was observed for 2.5 hr with the compact D configuration. This configuration is best suited for deep integration and coarse mapping (resolution $\sim 3\farcs7$ at 100 GHz and $\sim 1\farcs6$ at 230 GHz) and provides the lowest phase noise and highest sensitivity. The source 3C 273 is chosen to calibrate the bandpass, while the sources J0851+202 and J0923+282 are chosen to calibrate the phase. The CO(J = 1–0) rest frequency is 115.271 GHz (the redshifted frequency is 114.643 GHz). We observed the emission line with the receivers set to a 3 mm band tunable sky frequency between 70.4 and 119.9 GHz. The receiver band has dual-polarization capabilities and each of the two polarizations delivers a bandwidth of 7.744 GHz in the lower sideband and upper sideband simultaneously. Each sideband contains two adjacent basebands of ~3.9 GHz width, called the inner and outer baseband. The spectral resolution is ~2 MHz throughout the wide sidebands.

3.2. The Data Reduction and $M_{\rm H_2}$

The CO(J = 1–0) line data are calibrated by *CLIC*, a module of the available *GILDAS* software package. We choose the channels from −860 to 400 km s^{-1}, which is a wide enough range to analyze the CO(J = 1–0) line. The final channels are smoothed to 10 km s^{-1}. The cleaning of the line image is done by the mapping module of *GILDAS* and the resulting channel map is shown in the left panel of Figure 6. The synthesized beam size is $10\farcs62 \times 4\farcs76$. The uncertainty of calibration in the flux is ~20% and the 1σ uncertainty is about ~5.6 mJy/beam. The reference center of the map is set to be the same as the optical center so that we can compare the relative positions of Hα and CO(J = 1–0); (see the right panel of Figure 6). We can see that the emission of CO(J = 1–0) is mainly concentrated at SF and TPSB regions and basically overlaps the emission of Hα. We do

[5] http://users.obs.carnegiescience.edu/gblancm/izi

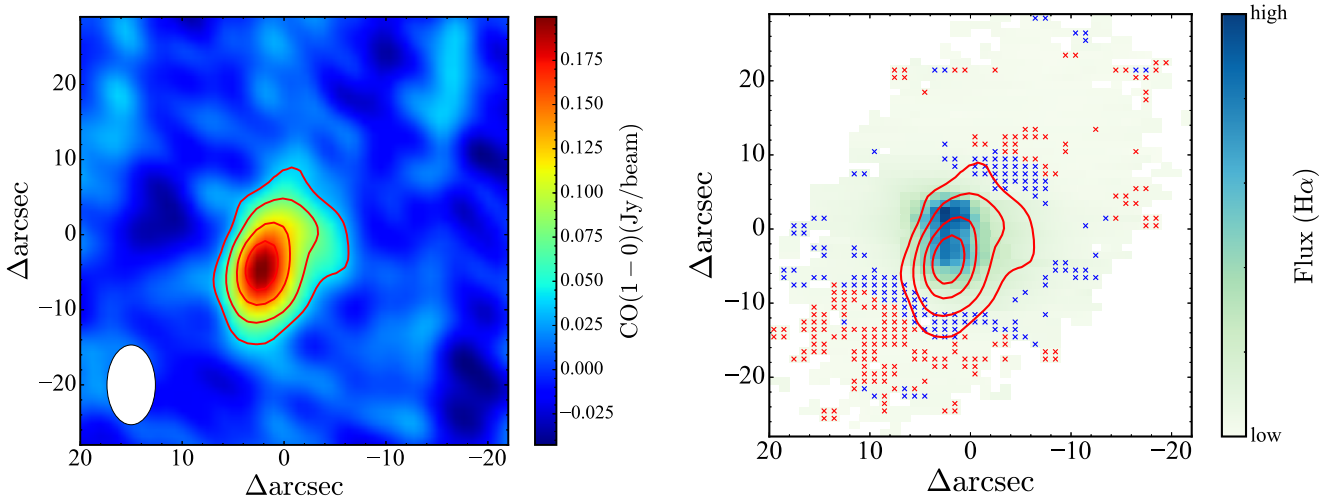

Figure 6. Left panel: the image of NOEMA CO(J = 1–0) emission. The synthesized beam size is $10\farcs62 \times 4\farcs76$ as marked in the lower-left corner. Right panel: image of Hα overlaid with NOEMA CO(J = 1–0) contours. The levels of the contours are 0.04, 0.08, 0.13, and 0.17. The red and blue crosses are the same as in Figure 2. The reference coordinates of the two panels have been set in the same scale to show clearly the relative positions of Hα and molecular gas regions.

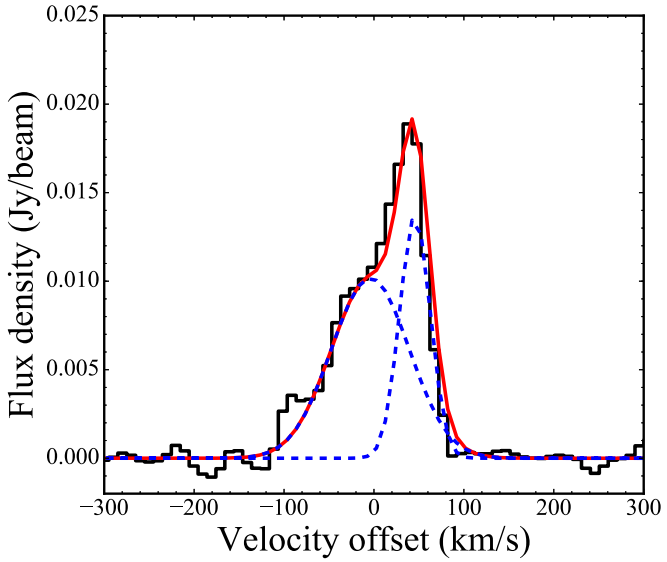

Figure 7. Decomposition of the CO(J = 1–0) line profile, smoothed to a resolution of 10 km s^{-1}. The black line represents the original spectrum and the blue dashed lines Gaussian models. The red solid line is the best-fit model, the superposition of the two Gaussian profiles.

not detect CO(J = 1–0) emission in the QPSB regions, but weak emission exists in the TPSB region. In addition, we find that there is an offset between the peaks of the optical and the millimeter CO emission (see the detailed description in Section 4.4).

We extract the CO(J = 1–0) emission of each spaxel with enough S/N (3σ) at the peak and construct a stacked spectrum (Figure 7). The interesting point is that the CO(J = 1–0) line shows asymmetry in its profile. We fit the spectrum with two Gaussians. One of them represents the redshift component, while the other represents the rotation component. It is found that one of the Gaussians shows a redshift of $\sim$46 km s^{-1}, which might indicate the inflow of gas, while the other does not. The asymmetrical profile does not disappear even though we stack the spectra within an effective radius. The flux density of CO(J = 1–0) emission is estimated from the best-fit model.

We use the relation given by Solomon & Vanden Bout (2005) to calculate the luminosity of CO(J = 1–0):

$$L'_{\rm CO} = 3.25 \times 10^7\, S_{\rm CO}\Delta v\, \nu_{\rm obs}^{-2}\, D_L^2\, (1+z)^{-3} \quad (3)$$

where $S_{\rm CO}\Delta v$, $\nu_{\rm obs}$, and D_L are the CO integrated flux density in units of Jy km s^{-1}, the observing frequency in GHz, and the luminosity distance in Mpc, respectively.

The mass of molecular hydrogen ($M_{\rm H_2}$) is estimated using following formula:

$$M_{\rm H_2} = \alpha_{\rm CO} \times L'_{\rm CO} \quad (4)$$

where $\alpha_{\rm CO}$ is the conversion factor between CO(J = 1–0) and H_2. Combining the $\Sigma_{\rm H\,I}$ derived in Section 2.4, the inclination-corrected $\Sigma_{\rm gas}$ ($\Sigma_{\rm H\,I+H_2}$) is estimated by adopting $\alpha_{\rm CO} = 4.3\, M_\odot\, ({\rm K\,km\,s^{-1}\,pc^2})^{-1}$, for the inner disk of Galaxy (Bolatto et al. 2013).

4. Results and Discussion

4.1. The Star Formation and Metallicity in PGC 26218

Figure 8 shows the map of SFR in logarithmic space for PGC 26218. It is found that star formation occurs mainly in an effective radius, which is consistent with the distribution of CO emission. As mentioned in Figure 7, the redshift component might indicate gas inflow, which could have led to the star formation in the central region.

Previous studies have shown that the stellar mass surface density within the central 1 kpc, Σ_1, strongly correlates with the star formation (Cheung et al. 2012; Fang et al. 2013; Luo et al. 2019). In order to compare our result to Fang et al. (2013), we also adopt the stellar mass from the MPA-JHU DR7 catalog ($\log M_* = 9.15$) and a similar method to estimate Σ_1. Here, we estimate Σ_1 from the NASA-Sloan Atlas catalog providing the surface brightness profiles in a series of angular sizes. The extinction-corrected and k-corrected surface brightness profiles within 1 kpc in i-band are used to convert to Σ_1 according to the mass-to-light ratio of the i-band (see Fang et al. 2013 for detailed calculations). The value of log Σ_1 for PGC 26218 is 8.25 $M_\odot\,{\rm kpc}^{-2}$ (see Table 2), which is 0.34 dex ($\sim 2\sigma$) below the best-fitting relation of Σ_1–M_* obtained from the

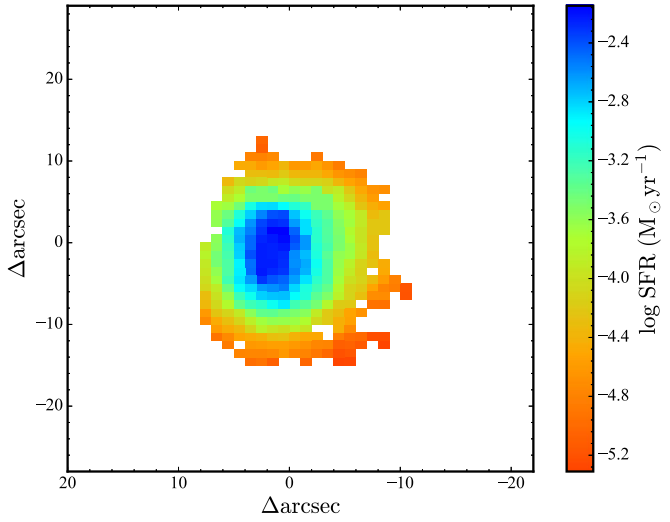

Figure 8. Spatial distribution of SFR for PGC 26218.

combination of blue and green valley galaxies (Fang et al. 2013). We also extract the mass value within 1 kpc from the stellar population analysis method and find that the value of Σ_1 does not change significantly. The position of PGC 26218 in the Σ_1–M_* relation suggests that the central star formation might not be suppressed significantly. With the current SFR, the remaining molecular gas can last for about 0.1 Gyr.

4.2. SFMS and K–S Law

The SFMS (Elbaz et al. 2007; Salim et al. 2007) shows the relationship between stellar mass and SFR. S0 galaxies are often thought to have an absence of noticeable star formation regions. To investigate whether PGC 26218 resides in the SFMS, we put the source on the SFMS relation given by Elbaz et al. (2007), who obtained SFR and stellar mass from the MPA-JHU DR4 catalog.[6] It is noted that the SFMS in Elbaz et al. (2007) was calibrated based on a Salpeter (1955) IMF. So, we adopt here $\log M_* = 9.32$ to investigate the position of PGC 26218 in the SFMS. We find PGC 26218 deviates slightly from the best-fitting relationship (slightly below the SFMS), but it follows the SFMS relation well within the error range. Speagle et al. (2014) gave a redshift-dependent SFMS relation using a compilation of many studies from the literature. We find that PGC 26218 still follows the redshift-dependent SFMS relation considering 0.2 dex scatter.

The tight relationship between $\Sigma_{\rm gas}$ and $\Sigma_{\rm SFR}$ (i.e., the K–S law) has been found in different types of star-forming galaxies (Schmidt 1959; Kennicutt 1998b; Kennicutt & Evans 2012). Figure 9 displays the K–S law for ETGs, star-forming, and starburst galaxies. We find that the ETGs (green points, most of them are S0 galaxies) in Davis et al. (2014) deviate from this relationship, while PGC 26218 (red point) basically obeys the K–S law, which implies that some mechanisms enhance its SFR. It is noted that $\Sigma_{\rm SFR}$ is computed in the same region as the CO(J = 1–0) measurement (see Section 3.2). We find that the result will not change if we compute $\Sigma_{\rm SFR}$ and $\Sigma_{\rm gas}$ in an effective radius. Although the fraction of molecular gas for PGC 26218 (∼2%) is slightly lower than that of Davis et al. (2014) (∼3%), the star formation efficiency in PGC 26218 might be higher. Wei et al. (2010) presented the relationship

[6] http://www.mpagarching.mpg.de/SDSS/DR4/

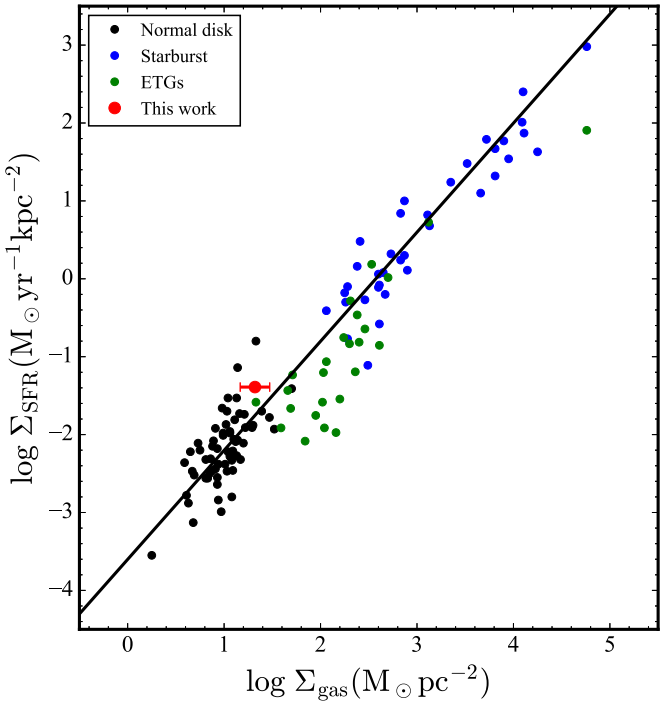

Figure 9. Relationship between log $\Sigma_{\rm gas}$ and log $\Sigma_{\rm SFR}$. The green points represent the ATLAS^{3D} ETGs with spatially resolved CO(J = 1–0) detections from Davis et al. (2014), while black and blue points represent the normal and starburst galaxies form Kennicutt (1998b), respectively. The solid line is the line of best fit for the Kennicutt (1998b) sample. PGC 26218 is marked in red.

between molecular gas and star formation in low-mass ellipticals/S0 galaxies. They found that most blue-sequence ellipticals/S0 galaxies show higher $\Sigma_{\rm SFR}$ at fixed $M_{\rm H_2}$, which is similar to local dwarf galaxies. In addition, the fraction of molecular gas is a factor of 2 higher than that of PGC 26218. Kokusho et al. (2017) studied the star formation of the same sample as Davis et al. (2014) in the ATLAS^{3D} survey. They found that the local ETGs have a similar star formation efficiency to the star-forming galaxies and follow the K–S law. The difference between them might be attributed to the methods of calculating SFR. Davis et al. (2014) calculated the SFR via the far-UV and 22 μm, while Kokusho et al. (2017) did so via spectral energy distribution fitting. Colombo et al. (2018) combined the CO observations made by the Combined Array for Millimeter-wave Astronomy from Extragalactic Database for Galaxy Evolution survey (Bolatto et al. 2017) with the 2D-spectroscopic observations made by CAHA from the Calar Alto Legacy Integral Field Area survey (Sánchez et al. 2012). They calculated $\Sigma_{\rm SFR}$ from the Hα map and investigated the dependence of $\Sigma_{\rm SFR}$ on Hubble types. They found that S0 galaxies have lower $\Sigma_{\rm SFR}$ than that of spirals, which is inconsistent with PGC 26218.

4.3. Kinematics of Stars and Gas

Within the region of CO(J = 1–0) emission, we compare the kinematics of stars, Hα, and CO(J = 1–0). Figure 10 shows the distributions of the line-of-sight velocities for these three components. The major axis of stellar, Hα, and CO(J = 1–0) velocity fields (dashed lines in Figure 10) are measured using the KINEMETRY code (Krajnović et al. 2006). We define the position angles as the counterclockwise angle between north and a line that bisects the velocity field of gas or stars on the

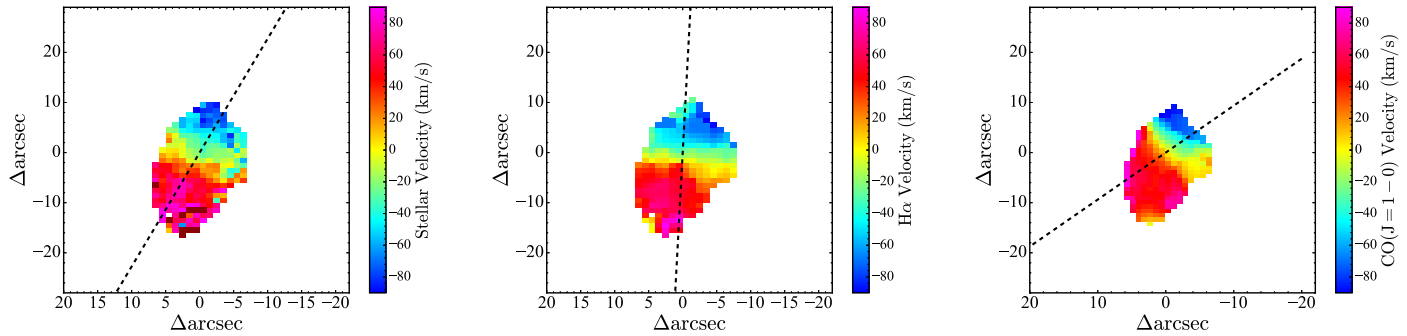

Figure 10. Maps of velocities for stars (left panel), ionized gas (middle panel), and CO(J = 1–0); (right panel). The dashed lines represent the major axis of rotation.

Figure 11. The *GALFIT* fitting for only the disk component in the SDSS r-band. The data image, model image, and residual image are shown from left to right, respectively.

receding side. We find that the major axis of stellar, Hα, and CO(J = 1–0) velocities are 156° ± 2°, 178° ± 4°, and 133° ± 10°, respectively. The difference in rotation axes between Hα and CO(J = 1–0) is larger than 45°. In addition, we find that the velocity of CO(J = 1–0) displays an asymmetry, which indicates that the gas has a motion relative to the stellar components. In general, the kinematic misalignment between ionized gas and CO(J = 1–0) implies that the fuel for star formation might come from the external environment.

4.4. Multiple Nuclear Structures and the Origins of Star Formation

George (2017) found that star-forming ellipticals/S0 galaxies display the features of gas-rich minor mergers that fuel the central star formation. The above results give us the motivation to explore the mechanisms causing PGC 26218 to undergo a burst of star formation.

The morphological disturbations of galaxies can give us clues into the origins of nuclear activities. In order to investigate the central structure of PGC 26218, we simply use a disk component (Sérsic index = 1) to model the galaxy disk of PGC 26218 in the r-band (Figure 11). We can clearly see from the residual image that PGC 26218 displays a peculiar structure at its center. It is worth noting that the peculiar structure in the residual image does not disappear even though we use two components (i.e., bulge and disk components) to decompose the r-band image. The Sérsic indices of bulge and disk are 1.2 and 1.0, respectively. In order to highlight the

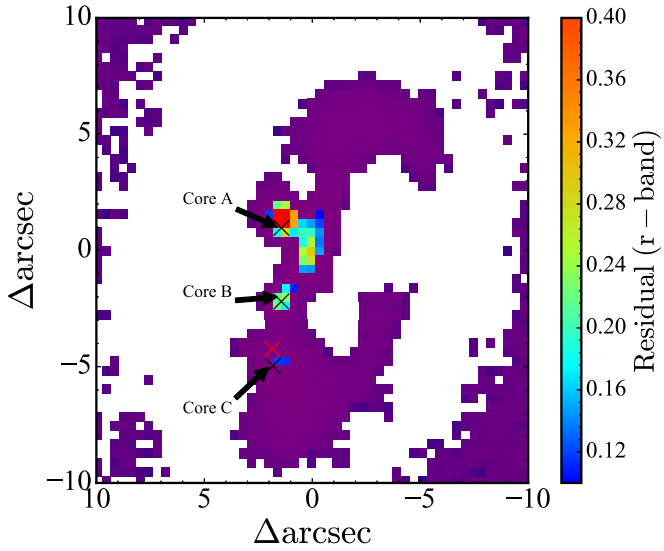

Figure 12. Same residual image as in Figure 11. The center of the image is the same as in Figure 2. Three black crosses represent the positions of cores defined by us and the red cross indicates the center of CO(J = 1–0) emission. The region is marked in purple if the residual is lower than 0.1.

structure of the central region, we compute only the disk component assuming a pure disk model. Figure 12 highlights the disk-subtracted residual image. We find PGC 26218 shows extreme morphological peculiarities that may be triggered by a galactic merger. We mark the positions with the highest flux

compared with surroundings as core a, core b, and core c in the *r*-band, respectively. It is found that the projected distances between core a and core b, core a and core c, and core b and core c are 3.″2 (0.35 kpc), 6.″0 (0.65 kpc), and 2.″8 (0.31 kpc), respectively. The peak of CO($J = 1$–0) nearly overlaps core c and it lies ∼0.6 kpc from the center of Hα (i.e., core a). However, we should keep in mind that the offset is comparable to the resolution of CO($J = 1$–0). Higher resolution observations are needed to resolve this question.

Actually, many previous studies have presented the presence of multiple optical nuclei in PGC 26218. Mazzarella & Boroson (1993) presented the properties of over 100 Markarian galaxies with multiple nuclear structures or peculiar morphologies. They used the software IMAGES to measure the structure of nuclei and found that PGC 26218 (Mrk 1230 in their paper) shows extended nuclear structure along the major axis. Nordgren et al. (1995) studied the morphologies and kinematics of 16 Markarian galaxies. Their results suggested that PGC 26218 has three nuclei and the farthest and nearest projected distances between two nuclei are 1.2 kpc and 0.5 kpc, respectively. In addition, PGC 26218 is also included in Gimeno et al. (2004) as a double nucleus case. They found that the separation between the two nuclei is about 0.4 kpc. We note that if the two nuclei depicted by Gimeno et al. (2004) are the a and b components in our Figure 12, then the projected separation estimated by us agrees well with theirs.

There are several scenarios that can be used to explain the occurrence of central star formation activity. (i) Internal secular evolution, such as the turbulence of a bar (Pfenniger & Norman 1990). The presence of a bar causes the gas to inflow to the center, thus inducing the starburst and fueling the mass concentration. In this scenario, the vigorousness of the starburst induced by the bar depends on the stellar mass. Carles et al. (2016) suggested that massive ($M_* > 2 \times 10^{10} M_\odot$) barred galaxies more easily consume gas by bar-induced starbursts than low-mass barred galaxies. We do not expect that the starburst that occurred several hundred Myr ago was triggered by a bar because we do not find a prominent bar component in such a low-mass S0 galaxy. (ii) Disk instability. The instability of a gas-rich disk may lead to the formation of star-forming clumps, which can lose angular momentum due to interactions and fall toward the center of the galaxy (Elmegreen et al. 2008; Dekel et al. 2009). The observational evidence shows that the dissipational processes triggered by disk instabilities are expected to occur in massive galaxies in earlier cosmic times where there is a higher gas fraction than that of local universe (Bouché et al. 2007; Daddi et al. 2010). However, we do not expect a large amount of disturbed gas to be conserved in such a low-mass, low-z S0 galaxy because the current fraction of molecular gas mass is only ∼2% of the stellar mass and the galaxy has relatively regular rotations in its stellar and gas disks. (iii) Major and minor mergers. Cosmological hydrodynamic simulations show that the frequency of major mergers declines with the cosmic time (Maller et al. 2006). They found that the average merger rate of massive galaxies is 0.054 Gyr^{-1} at $z \sim 0.3$, and is 0.018 Gyr^{-1} for low-mass galaxies. It is believed that major mergers may be too destructive to preserve the inner components and regular disks. Minor mergers are expected to significantly increase the SFR (Saintonge et al. 2012; Kaviraj 2014) although they are not as violent as major mergers. At low redshift, the incidence of minor mergers is higher than that of major mergers and the minor mergers can build bulges without destroying disk structure. As suggested by Eliche-Moral et al. (2011), minor mergers can explain the existence of multiple inner components in unbarred galaxies, although this mechanism is more complex than other processes (such as bars and ovals, Kormendy & Kennicutt 2004). Eliche-Moral et al. (2018) have studied whether galaxy mergers can reproduce the features of S0-like remnants based on the GalMer simulated database. They suggested that the mergers can result in relaxed morphologies and inner subcomponents, such as ovals, lenses, and compact sources. Furthermore, the relics are more durable in minor mergers than in major mergers. For PGC 26218, a minor merger leads to the slow rearrangement of gas from the disk to the center of galaxy and this progress has not yet been completed (as indicated by the multiple nuclear structures we see).

Bellstedt et al. (2017) studied stellar kinematics of four S0 galaxies with $M_* \gtrsim 10^{10} M_\odot$ utilizing the DEIMOS instrument on the Keck telescope. They found that these S0 galaxies generally resemble spiral progenitors more than merger remnants. Although they suggested that these S0 galaxies are likely formed via faded disks, merger events cannot be ruled out for the formation of S0 galaxies. Fraser-McKelvie et al. (2018) investigated the relative importance of gas stripping and mergers using 279 S0 galaxies from the MaNGA (Mapping Nearby Galaxies at APO) survey (Bundy et al. 2015). They found that the bulges of low-mass S0 galaxies are almost always younger than their disks, which is consistent with PGC 26218. However, they contributed it to bulge rejuvenation or disk fading. Temi et al. (2009) studied star formation using a sample of local ETGs from the Spectroscopic Areal Unit for Research on Optical Nebulae survey (Bacon et al. 2001). They found that the cold gas for star formation in S0 galaxies is created via stellar mass loss. A similar result has been found by Shapiro et al. (2010). Furthermore, they also suggested that the minor mergers might be building up the bulges of red sequence S0 galaxies. Kaviraj et al. (2009, 2010) studied the importance of minor mergers in low-level star formation of ETGs. They found that minor mergers are the main mechanism driving star formation at low redshift. Méndez-Abreu et al. (2019) studied the star formation of local S0 galaxies with $M_* \gtrsim \times 10^{10} M_\odot$ from the CALIFA survey. Their results show that the star formation in bulges is significantly lower than that in disks. This contradiction to our result might be attributed to the type of bulge because a larger bulge is more likely to quench star formation in the central region via the morphological, but related with mass, quenching scenario. This can be also understood by differences of peculiar objects (as their NGC 3773 case) from the general trend of low-mass objects ($M_* < 10^{10} M_\odot$) as seen in the dispersion in the derived stellar population properties in the low-mass range (García-Benito et al. 2017).

In summary, PGC 26218 is a good case to connect the relevance between minor mergers in the past and star formation in the present, together with the evolutionary trajectories of S0 galaxies. We suggest by combining the results in this work with those of previous studies that PGC 26218 could have undergone a gas-rich minor merger, which triggered the starburst at the outskirts a few hundred Myr ago and the central star formation activity as indicated by the multiple nuclear structures.

5. Summary

We have studied the physical properties of a nearby S0 galaxy with the features of nuclear star-forming activity and post-starburst features in the disk. Based on optical IFU spectroscopic observations from CAHA and millimeter observations from NOEMA, we have established a possible connection between a starburst that happened several hundred Myr ago, nuclear star formation activity, extreme morphological peculiarity, and a minor merger. Our main results are summarized as follows:

1. Based on IFU spectroscopic observations, the S0 galaxy PGC 26128 shows properties of post-starburst features at the outskirts with star formation in the central region. The ongoing star formation prevents the S0 galaxy from deviating from the SFMS.
2. The SFR and the log $M_{\rm H_2}$ of PGC 26218 are 0.28 $M_\odot\,{\rm yr}^{-1}$ and 7.60 $M_\odot$, respectively. With this mass of molecular hydrogen, the star formation of PGC 26218 can last about 0.1 Gyr. PGC 26218 obeys the K–S law as well as normal disk galaxies and starburst galaxies. The question is whether this class of galaxy is common, which needs to be further explored with a large sample of S0 galaxies in local universe.
3. We find that the rotation axes of stars, ionized gas, and CO(J = 1–0) differ by more than 20°, respectively. The difference between ionized gas and CO(J = 1–0) reaches 45°, which indicates that the fuel that allows PGC 26218 to form stars might come from the surrounding environment.
4. PGC 26218 has multiple nuclear structures in its optical SDSS image and the CO(J = 1–0) emission line shows an asymmetric profile (with a 46 km s^{-1} redshift component). These results indicate that this galaxy may have undergone a gas-rich minor merger, which triggered the starburst a few hundred Myr ago and swept gas into the center, leading to the star formation.
5. There is an offset between the centers of Hα and CO(J = 1–0) with a projected offset of 0.6 kpc. However, the offset should be further investigated by higher resolution observations because this offset is comparable to the beam size semimajor axis.

This work is supported by the National Key Research and Development Program of China (No. 2017YFA0402703) and by the National Natural Science Foundation of China (No. 11733002). In addition, we acknowledge the support of the staff from CAHA and NOEMA. Rubén García-Benito acknowledges financial support from the Spanish Ministry of Economy and Competitiveness through grant 205 AYA2016-77846-P. Rubén García-Benito acknowledges support from the State Agency for 206 Research of the Spanish MCIU through the "Center of Excellence Severo Ochoa" award to 207 the Instituto de Astrofísica de Andalucía (SEV-2017-0709).

ORCID iDs

Xue Ge https://orcid.org/0000-0002-8348-2783
Qiu-Sheng Gu https://orcid.org/0000-0002-3890-3729
Rubén García-Benito https://orcid.org/0000-0002-7077-308X

References

Abazajian, K. N., Adelman-McCarthy, J. K., Agüeros, M. A., et al. 2009, ApJS, 182, 543
Aguerri, J. A. L., Balcells, M., & Peletier, R. F. 2001, A&A, 367, 428
Alatalo, K., Cales, S. L., Rich, J. A., et al. 2016, ApJS, 224, 38
Aragón-Salamanca, A., Bedregal, A. G., & Merrifield, M. R. 2006, A&A, 458, 101
Bacon, R., Copin, Y., Monnet, G., et al. 2001, MNRAS, 326, 23
Baldwin, J. A., Phillips, M. M., & Terlevich, R. 1981, PASP, 93, 5
Balogh, M. L., Miller, C., Nichol, R., Zabludoff, A., & Goto, T. 2005, MNRAS, 360, 587
Balogh, M. L., Morris, S. L., Yee, H. K. C., Carlberg, R. G., & Ellingson, E. 1999, ApJ, 527, 54
Barway, S., Wadadekar, Y., Vaghmare, K., et al. 2013, MNRAS, 432, 430
Bedregal, A. G. 2007, arXiv:astro-ph/0702125
Bekki, K. 1998, ApJL, 502, L133
Bekki, K., & Couch, W. J. 2011, MNRAS, 415, 1783
Bellstedt, S., Forbes, D. A., Foster, C., et al. 2017, MNRAS, 467, 4540
Blake, C., Pracy, M. B., Couch, W. J., et al. 2004, MNRAS, 355, 713
Blanc, G. A., Kewley, L., Vogt, F. P. A., & Dopita, M. A. 2015, ApJ, 798, 99
Bolatto, A. D., Wolfire, M., & Leroy, A. K. 2013, ARA&A, 51, 207
Bolatto, A. D., Wong, T., Utomo, D., et al. 2017, ApJ, 846, 159
Bouché, N., Cresci, G., Davies, R., et al. 2007, ApJ, 671, 303
Brinchmann, J., Charlot, S., White, S. D. M., et al. 2004, MNRAS, 351, 1151
Bundy, K., Bershady, M. A., Law, D. R., et al. 2015, ApJ, 798, 7
Calzetti, D., Armus, L., Bohlin, R. C., et al. 2000, ApJ, 533, 682
Cappellari, M. 2017, MNRAS, 466, 798
Cappellari, M., & Copin, Y. 2003, MNRAS, 342, 345
Cappellari, M., & Emsellem, E. 2004, PASP, 116, 138
Cardelli, J. A., Clayton, G. C., & Mathis, J. S. 1989, ApJ, 345, 245
Carles, C., Martel, H., Ellison, S. L., & Kawata, D. 2016, MNRAS, 463, 1074
Cheung, E., Faber, S. M., Koo, D. C., et al. 2012, ApJ, 760, 131
Cid Fernandes, R., Stasińska, G., Schlickmann, M. S., et al. 2010, MNRAS, 403, 1036
Colombo, D., Kalinova, V., Utomo, D., et al. 2018, MNRAS, 475, 1791
Daddi, E., Bournaud, F., Walter, F., et al. 2010, ApJ, 713, 686
Davis, T. A., Rowlands, K., Allison, J. R., et al. 2015, MNRAS, 449, 3503
Davis, T. A., Young, L. M., Crocker, A. F., et al. 2014, MNRAS, 444, 3427
Dekel, A., Sari, R., & Ceverino, D. 2009, ApJ, 703, 785
Doe, S., Nguyen, D., Stawarz, C., et al. 2007, adass XVI, 379, 543
Dressler, A., Oemler, A., Jr., Poggianti, B. M., et al. 2013, ApJ, 770, 62
Elbaz, D., Daddi, E., Le Borgne, D., et al. 2007, A&A, 468, 33
Eliche-Moral, M. C., Balcells, M., Aguerri, J. A. L., & González-García, A. C. 2006, A&A, 457, 91
Eliche-Moral, M. C., González-García, A. C., Balcells, M., et al. 2011, A&A, 533, A104
Eliche-Moral, M. C., Rodríguez-Pérez, C., Borlaff, A., Querejeta, M., & Tapia, T. 2018, A&A, 617, A113
Elmegreen, B. G., Bournaud, F., & Elmegreen, D. M. 2008, ApJ, 688, 67
Fang, J. J., Faber, S. M., Koo, D. C., & Dekel, A. 2013, ApJ, 776, 63
Fraser-McKelvie, A., Aragón-Salamanca, A., Merrifield, M., et al. 2018, MNRAS, 481, 5580
Freeman, P., Doe, S., & Siemiginowska, A. 2001, Proc. SPIE, 4477, 76
García-Benito, R., González Delgado, R. M., Pérez, E., et al. 2017, A&A, 608, A27
García-Benito, R., Zibetti, S., Sánchez, S. F., et al. 2015, A&A, 576, A135
George, K. 2017, A&A, 598, A45
Gimeno, G. N., Díaz, R. J., & Carranza, G. J. 2004, AJ, 128, 62
González Delgado, R. M., Cid Fernandes, R., Pérez, E., et al. 2016, A&A, 590, A44
Goto, T. 2005, MNRAS, 357, 937
Goto, T. 2007, MNRAS, 381, 187
Governato, F., Brook, C. B., BrooK-S, A. M., et al. 2009, MNRAS, 398, 312
Hogg, D. W., Masjedi, M., Berlind, A. A., et al. 2006, ApJ, 650, 763
Hubble, E. P. 1926, ApJ, 64, 321
Husemann, B., Jahnke, K., Sánchez, S. F., et al. 2013, A&A, 549, A87
Johnston, E. J., Aragón-Salamanca, A., Merrifield, M. R., et al. 2014, ASP Conf. Ser. 480, Structure and Dynamics of Disk Galaxies (San Francisco, CA: ASP), 161
Jungwiert, B., Combes, F., & Palouš, J. 2001, A&A, 376, 85
Kauffmann, G., Heckman, T. M., Tremonti, C., et al. 2003a, MNRAS, 346, 1055
Kauffmann, G., Heckman, T. M., White, S. D. M., et al. 2003b, MNRAS, 341, 33
Kaviraj, S. 2014, MNRAS, 440, 2944
Kaviraj, S., Ellis, R., Yi, S., et al. 2010, Stellar Populations—Planning for the Next Decade, 168
Kaviraj, S., Peirani, S., Khochfar, S., et al. 2009, MNRAS, 394, 1713
Kaviraj, S., Schawinski, K., Devriendt, J. E. G., et al. 2007, ApJS, 173, 619
Kennicutt, R. C., & Evans, N. J. 2012, ARA&A, 50, 531
Kennicutt, R. C., Jr. 1998a, ARA&A, 36, 189

Kennicutt, R. C., Jr. 1998b, ApJ, 498, 541
Kewley, L. J., Dopita, M. A., Sutherland, R. S., Heisler, C. A., & Trevena, J. 2001, ApJ, 556, 121
Kewley, L. J., Groves, B., Kauffmann, G., & Heckman, T. 2006, MNRAS, 372, 961
Kokusho, T., Kaneda, H., Bureau, M., et al. 2017, A&A, 605, A74
Kormendy, J., & Bender, R. 2012, ApJS, 198, 2
Kormendy, J., & Kennicutt, R. C., Jr. 2004, ARA&A, 42, 603
Krajnović, D., Cappellari, M., de Zeeuw, P. T., & Copin, Y. 2006, MNRAS, 366, 787
Kroupa, P. 2001, MNRAS, 322, 231
Lacerda, E. A. D., Cid Fernandes, R., Couto, G. S., et al. 2018, MNRAS, 474, 3727
Laurikainen, E., Salo, H., Buta, R., et al. 2006, AJ, 132, 2634
Laurikainen, E., Salo, H., Buta, R., et al. 2010, MNRAS, 405, 1089
Lee, J. L., & Brunner, R. J. 2015, arXiv:1512.01204
Levesque, E. M., Kewley, L. J., & Larson, K. L. 2010, AJ, 139, 712
Luo, Y., Faber, S. M., Rodriguez-Puebla, A., et al. 2019, arXiv:1908.08055
Maller, A. H., Katz, N., Kereš, D., Davé, R., & Weinberg, D. H. 2006, ApJ, 647, 763
Mazzarella, J. M., & Boroson, T. A. 1993, ApJS, 85, 27
Méndez-Abreu, J., Sánchez, S. F., & de Lorenzo-Cáceres, A. 2019, MNRAS, 488, L80
M. J., & C. J. A. R. 1936, Sci, 84, 509
Moore, B., Katz, N., Lake, G., Dressler, A., & Oemler, A. 1996, Natur, 379, 613
Moore, B., Lake, G., & Katz, N. 1998, ApJ, 495, 139
Nordgren, T. E., Helou, G., Chengalur, J. N., Terzian, Y., & Khachikian, E. 1995, ApJS, 99, 461
Pawlik, M. M., Taj Aldeen, L., Wild, V., et al. 2018, MNRAS, 477, 1708
Peng, C. Y., Ho, L. C., Impey, C. D., & Rix, H.-W. 2002, AJ, 124, 266
Pfenniger, D., & Norman, C. 1990, ApJ, 363, 391
Poggianti, B. M., Aragón-Salamanca, A., Zaritsky, D., et al. 2009, ApJ, 693, 112
Querejeta, M., Eliche-Moral, M. C., Tapia, T., et al. 2015, A&A, 573, A78
Quintero, A. D., Hogg, D. W., Blanton, M. R., et al. 2004, ApJ, 602, 190
Rizzo, F., Fraternali, F., & Iorio, G. 2018, MNRAS, 476, 2137
Rowlands, K., Wild, V., Nesvadba, N., et al. 2015, MNRAS, 448, 258
Sage, L. J., & Welch, G. A. 2006, ApJ, 644, 850
Saha, K., & Cortesi, A. 2018, ApJL, 862, L12
Saintonge, A., Tacconi, L. J., Fabello, S., et al. 2012, ApJ, 758, 73
Salim, S., Rich, R. M., Charlot, S., et al. 2007, ApJS, 173, 267
Salpeter, E. E. 1955, ApJ, 121, 161
Sánchez, S. F., García-Benito, R., Zibetti, S., et al. 2016, A&A, 594, A36
Sánchez, S. F., Kennicutt, R. C., Gil de Paz, A., et al. 2012, A&A, 538, A8
Sánchez, S. F., Rosales-Ortega, F. F., Jungwiert, B., et al. 2013, A&A, 554, A58
Sánchez-Blázquez, P., Peletier, R. F., Jiménez-Vicente, J., et al. 2006, MNRAS, 371, 703
Sandage, A., Freeman, K. C., & Stokes, N. R. 1970, ApJ, 160, 831
Schawinski, K., Thomas, D., Sarzi, M., et al. 2007, MNRAS, 382, 1415
Schmidt, M. 1959, ApJ, 129, 243
Schruba, A., Bialy, S., & Sternberg, A. 2018, ApJ, 862, 110
Shapiro, K. L., Falcón-Barroso, J., van de Ven, G., et al. 2010, MNRAS, 402, 2140
Solomon, P. M., & Vanden Bout, P. A. 2005, ARA&A, 43, 677
Speagle, J. S., Steinhardt, C. L., Capak, P. L., et al. 2014, ApJS, 214, 15
Tapia, T., Eliche-Moral, M. C., Aceves, H., et al. 2017, A&A, 604, A105
Temi, P., Brighenti, F., & Mathews, W. G. 2009, ApJ, 695, 1
Tremonti, C. A., Heckman, T. M., Kauffmann, G., et al. 2004, ApJ, 613, 898
van Driel, W., & van Woerden, H. 1991, A&A, 243, 71
Vazdekis, A., Sánchez-Blázquez, P., Falcón-Barroso, J., et al. 2010, MNRAS, 404, 1639
Vergani, D., Zamorani, G., Lilly, S., et al. 2010, A&A, 509, A42
Wei, L. H., Vogel, S. N., Kannappan, S. J., et al. 2010, ApJL, 725, L62
Welch, G. A., & Sage, L. J. 2003, ApJ, 584, 260
Welch, G. A., Sage, L. J., & Young, L. M. 2010, ApJ, 725, 100
Xiao, M.-Y., Gu, Q.-S., Chen, Y.-M., & Zhou, L. 2016, ApJ, 831, 63
Yesuf, H. M., Faber, S. M., Trump, J. R., et al. 2014, ApJ, 792, 84